RSC Advances

ROYAL SOCIETY OF CHEMISTRY

www.rsc.org/advances

Cite this: DOI: 10.1039/c0xx00000x

www.rsc.org/xxxxxx

ARTICLE TYPE

Self-assembled Zirconia Nanotube Arrays: Fabrication Mechanism, Energy Consideration and Optical Activity

Ahmad W. Amer[a], Seifallah M. Mohamed[a], Ahmed M. Hafez[a], Siham Y. AlQaradawi[b], Amina S. Aljaber[b] and Nageh K. Allam[a,*]

Received (in XXX, XXX) Xth XXXXXXXXX 20XX, Accepted Xth XXXXXXXXX 20XX
DOI: 10.1039/b000000x

We present a comprehensive roadmap for the precise control of the dimensions and optical properties of anodically fabricated zirconia nanotubes. The effects of anodization time, applied voltage, solvent composition, as well as fluoride and water contents are investigated. The length of the resulted nanotubes showed a strong dependence on the concentration and mobility of F^- ions, whilst O^{2-} ion content was found to play a key role in controlling the nanotube wall thickness. A new insight into the formation of Zirconia nanotubes is introduced and discussed based on the Point Defect Model (PDM). Also, the energy consumption in the fabrication process of the nanostructured electrodes is modelled based on the involved thermodynamics and kinetics aspects. The effect of the dimensions of the nanotubes on the optical characteristics of the arrays was studied using Finite Difference Time Domain (FDTD). The results show a decrease in transmittance with increasing the length and wall thickness, and decreasing the pore size of the nanotubes. The reported results provide deep insights into the structure-property relationships of ZrO_2 nanotubes, which will be of great help in large-scale industrial applications.

1 Introduction

With emerging nanoscale technologies, the need for developing efficient protocols for the synthesis of nanostructured materials that can be easily transferred to the industry has become dire. Indeed, such protocols have been established in many fields in order to satisfy application-specific requirements, including synthesis of nanoparticles,[1,2] nanowires,[3,4] nanotubes,[5-7] and other nanostructures.[8-10] For instance, efficient solar-driven water splitting through the use of nanotube photoanodes has been a challenge since the success of the Honda-Fujishima experiment.[11] Many factors, such as the aspect ratio, surface area, surface roughness, and wall thickness,[12,13] form specific criteria that must be met in order to achieve efficient hydrogen production.

In this sense, the field of metal oxide nanotube synthesis has gained special attention throughout the past 10 years, owing to the wide spectrum of applications that depend on their unique properties. zirconium dioxide (ZrO_2) nanostructures have emerged as a very promising member of the metal oxide nanotube family. The high stability and biocompatibility of ZrO_2 nanotubes allow their use as bio-active systems.[14-16] In addition, their wide band gap semiconducting properties can be utilized in multi-functional catalysis.[17-19]

One highly efficient and facile method for synthesizing ZrO_2 nanotubes is anodic oxidation *via* selective etching of zirconium foil in an electrochemical cell.[20,21] Such synthesis route has recently attracted wide attention following its success in the synthesis of the broadly used anodic aluminum oxide membranes (AAO),[22,23] where the ease of accurately manipulating nanotube structure and morphology through controlling the process parameters is possible. Furthermore, it is widely accepted that the anodization of Zr foils resembles to a great extent that of titanium foils.[20,24-26] To this end, many recent reports attempted to clearly identify the effect of process variables that enable the fabrication of well-defined ZrO_2 nanotubes. Lee *et al.*[21] studied the effect of applied voltage (10-30V) and anodization time (1-60 min) in a typical HF-based electrolyte on the properties of the resulted material. Vertically-aligned nanotubes were attained at 20V and 20 min. Schmuki *et al.*[25] reported the formation of highly-ordered ZrO_2 nanotube arrays at 20V and an anodization time of 1 hour using NH_4F as the etchant. However, using a very similar electrolyte/etchant composition, Zhao *et al.*[26] reported optimum results at 10V and 3 hrs of anodization time. Xuan-Yong *et al.*[27] studied the effect of fluoride-to-oxygen (F/O) ratio on the competing processes of chemical etching and anodic oxidation. As the F/O ratio was increased, the nanotubes became more structured and crystalline, and the array length increased until a certain threshold ratio (0.7), above which the nanotubes collapsed. However, the substantially high applied voltage in this study (80V) renders the process inefficient for large-scale use. Ismail *et al.*,[20] on the other hand, used a relatively low voltage of 20V to study the effect of fluoride content. Although the crystallinity improved as the amount of NH_4F added was increased, confirming Xuan-Yong's observations, the length of the synthesized arrays decreased with increasing fluoride content. Furthermore, the threshold content at which the nanotubes

collapsed changed with the decreased voltage. Muratore *et al.*[24] reported a higher optimum F/O ratio of 0.9 when changing the water content instead of the fluoride ion content. Adding more water increased the diameters of the resulted nanotubes by an order of ~20 nm. Although other studies attempt to shed the light on the combined effect of varying anodization variables,[28,29] more combinatorial studies are needed in order to reach a consensus with the optimum combination of process variables, thus taking the first steps towards formulating a market-reliable synthesis protocol for ZrO_2 nanotubes.

Herein, we report the effects of a combination of anodization process variables (time, applied voltage, electrolyte composition, fluoride and oxide ion contents) on the structure and morphology of ZrO_2 nanotube arrays. Also, mathematical models have been developed to account for the energy consumption during the fabrication process. Further, the effect of the dimensions of the synthesized nanotubes on their optical properties is investigated both experimentally and theoretically.

2 Experimental

Pure zirconium foils (Alfa Aesar, 99.8% purity) were ultrasonically cleaned in acetone/ethanol and distilled water, respectively. Anodization was done in a two-electrode cell with the zirconium foil as the working electrode and platinum as the counter electrode, in glycerol-based electrolytes containing variable amounts of formamide, H_2O, and NH_4F. The anodized area was fixed at 10x10 mm. The distance between the electrodes was fixed at 20 mm, and the operation temperature was fixed at room temperature (approximately 23˚C). Time-dependant anodization current was tracked on 5-minute intervals. Anodization was performed using an Agilent E3612A DC power supply. The morphology of the as-anodized samples was studied using a LEO Supra 55 Field Emission Scanning Electron Microscope (FESEM). Specimens were annealed in a LINDBURG Programmable Furnace model N41/M 29667. The crystal structure of as-anodized and annealed samples was studied using a PANalytical X'Pert PRO XRD diffractometer. The optical properties of the anodized foils were measured using a home-made setup that was installed into a Newport QE-PV-SI QE/IPCE instrument. Finite Difference Time Domain simulations were implemented on a computer-written code. The source used was a Gaussian pulse source having a central frequency (f_c) of 1498.96229 THz, and a pulse width (w) of 2997.92 THz. For detection, two observation planes were positioned at the top and the bottom of the nanotubes to measure the transmittance and the absorbance, respectively. A lorentzian model was used for simulating the permittivity-frequency plot, along with eye curve-fitting in order to match the simulation model with the experimental results done on ZrO_2 nanotubes.

3 Results and Discussion

3.1 Effect of Anodization Conditions

To study the effect of solvent composition on the competing processes of chemical etching and oxidation, Zr foils were anodized in glycerol-based electrolytes containing different formamide (FA) contents, while keeping the NH_4F and H_2O concentrations at 1wt% and 4wt%, respectively. Fig. S1 shows the resulted ZrO_2 nanotube arrays. Uniform nanotube arrays were obtained in electrolytes containing FA up to 40%. Note the changing morphology of the nanotubes from hexagonal in pure glycerol electrolyte (Fig. S1(a)), to circular nanotubes as FA content was increased to 10% and 20% (Fig. S1(b,c)), and back again to hexagonal shape at 30% and 40% FA (Fig. S1(d,e)). Note also that the most ordered nanotube arrays were obtained in electrolytes with 20% FA, Fig. 1(a). Notably, the top of the nanotubes grown in electrolytes with 10 and 30% FA were covered with debris, which basically consists of detached nanotubes that may have fallen off the substrate during post-anodization ultrasonic cleaning. The nanotubes grown in electrolytes containing 40% FA were covered with a 2μm-thick layer of amorphous material, which indicates corrosion of the top ends of the nanotubes as a result of the high F^- ion mobility.

Fig. 1(b) shows the variations of the lengths, diameters, and wall thicknesses of the nanotube arrays fabricated in electrolytes containing different FA contents. Note the increase in the nanotube length with increasing the FA content in the electrolyte from 10% to 30% followed by a plateau until 40% FA. At 50% FA, the Zr foil was cut into two pieces at the electrolyte/air interface. The nanotube wall thickness showed a similar behavior to the change in length. Nanotube diameter, on the other hand, showed a much earlier plateau (near 10%). Figure S1(f) shows the time-dependant anodization current curves for samples anodized in electrolytes containing different FA contents. Once the Zr foil is immersed in the electrolyte, the current increases until an insulating passive layer builds up (typically an oxide), resulting in a gradual decrease in current until reaching a steady state. The steady state current (I_{SS}) shows an ohmic dependence on the applied voltage (V) and the combined resistance of a bi-layer passive film as predicted by the second generation of the Point Defect Model,[30] i.e.

$$I_{SS} = \frac{V}{R_{OL}+R_{BL}} \quad (1)$$

where R_{OL} and R_{BL} are the resistances of the outer and barrier layers, respectively (see Section 3d). In addition, the initial anodization current increases as the FA content increases, as expected, due to the increased ion mobility[29] in the electrolyte owing to the lower viscosity of FA as compared to glycerol. In order to study the effect of different combinations of F^- and O^{2-} ion contents, Zr foils were anodized in glycerol-based electrolytes containing 20% FA and different F^- contents (0.5, 1, and 2 wt%), as well as different water contents (2, 3, and 4 wt%). Fig. 1(c) shows a representative FESEM image of the nanotubes grown in glycerol-based electrolyte containing 20% FA, 2 wt% NH_4F and 2 wt% H_2O. Fig. S2 (in the supporting information) shows the FESEM images of the as-grown nanotube arrays under the various F^- and O^{2-} ion contents. ZrO_2 nanotubes with hexagonal cross sections were observed for all etchant-water contents except for the nanotubes grown in electrolytes containing 1wt% NH_4F and 4wt% water. Furthermore, ZrO_2 nanotubes grown in electrolytes with 1wt% NH_4F and 2wt% water, as well as 2wt% NH_4F and 2wt% water showed long-range order throughout the substrate (Fig. 1(c)). It is important to note the presence of amorphous debris exclusively on the arrays anodized in all electrolytes containing 0.5wt% NH_4F (Fig. S2).

Fig. 1(d) is a 3-D plot showing the variation of nanotube

diameter with respect to H_2O and NH_4F contents. Increasing both F^- and O^{2-} ion concentrations in the electrolyte resulted in an

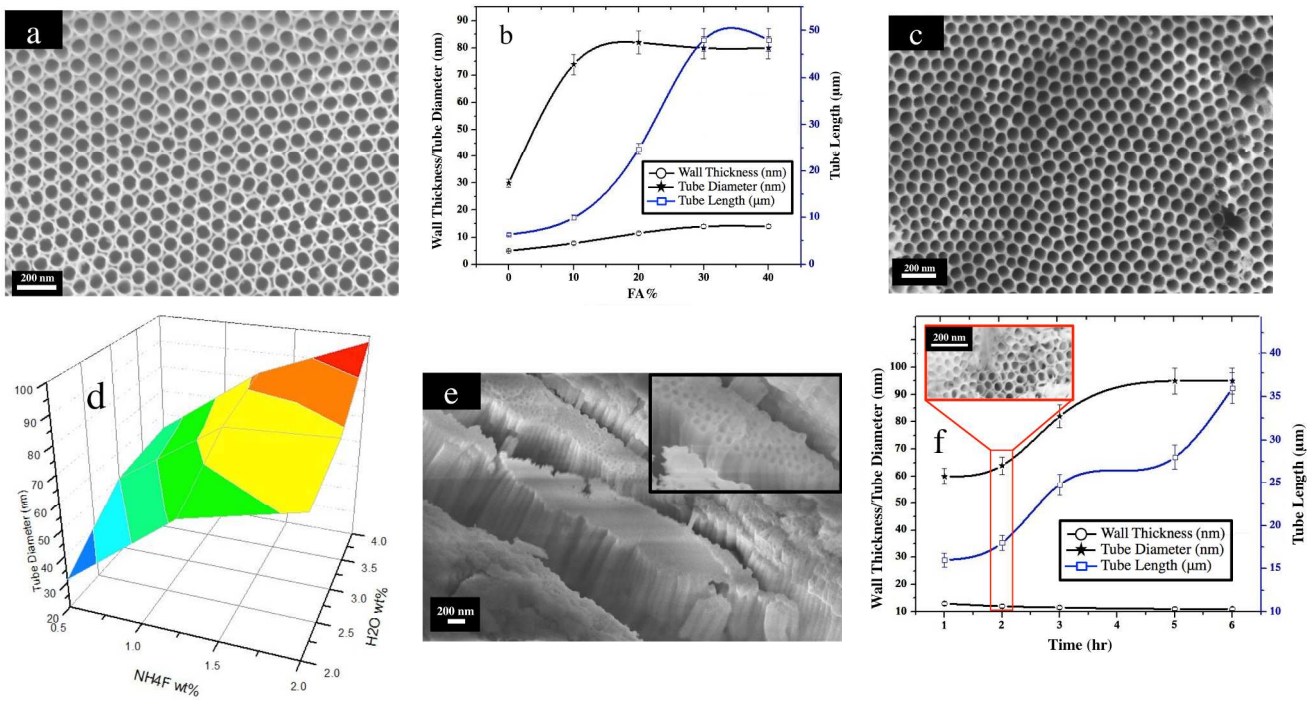

Fig. 1 (a) FESEM images of as-grown ZrO2 nanotube arrays via anodic oxidation for 3hrs @50V in glycerol electrolytes containing 20vol% FA, 4wt% H2O and 1wt% NH4F (b) Variation of the ZrO2 nanotube dimensions with FA content. (c) Same as panel (a) but with 2wt% H2O and 2wt% NH4F. (d) 3-D plot illustrating the effect of varying H2O and NH4F content in the electrolytes on the as-anodized ZrO2 nanotube diameters. (e) Same as panel (a) but under applied voltage of 30V. (f) Variation of ZrO2 nanotube dimensions with anodization time. Inset shows a representative FESEM image of the sample anodized for 2 h

increase in nanotube diameter. As the F^- ion content increased, nanotube length decreased, similar to the anodization of titanium foils.[37] Increasing O^- ion content, on the other hand, resulted in an increase in the nanotube length.

Anodization time was also varied for samples anodized in glycerol-based electrolytes containing 20% FA, with constant 4wt% H_2O and 1wt% NH_4F contents. Fig. 1(e) shows a representative FESEM image of the fabricated nanotubes after 3 hours of anodization. The full set of FESEM images for the nanotubes fabricated at various time intervals is shown in Fig. S3. Note that circular nanotubes were obtained for all anodization durations. Note also the presence of detached nanotubes/debris on the surfaces of the foils anodized for 2 hours. The nanotube growth rates shifted from 16μm/h for anodization time of 1 h to 8.5 μm/h for anodization time of 2hrs. This dramatic shift in the growth rate can be related to the nanotube detachment during the anodization process, where new nanotube arrays replace the detached ones, resulting in shorter nanotubes than expected. The nanotube growth rate of 8.3μm/h remained almost constant for the remaining anodization times (up to 16 h). Fig. 1(f) shows the effect of increasing anodization time on the dimensions of the resulted ZrO_2 nanotubes. The effect of anodization time on the nanotube length is fairly linear, as expected at the relatively slow etching rate in the 20% FA electrolyte. In addition, increasing anodization time has an effect on the nanotube diameter similar to that of increasing FA content in the electrolyte, such that more ions would reach the anode at the longer time span (or at higher FA content in the electrolyte). A steady state is reached near 4 h, which can be related to an equilibrium state between chemical etching and anodic oxidation at the top of the array. In contrast to increasing FA content, however, the wall thickness is decreasing as the anodization time increases, indicating a lower oxide layer growth rate as compared to the rate of chemical etching. This can be explained in terms of the added O^{-2} ions as FA content increases in the electrolyte.[27] This increase may be the reason behind the increasing wall thickness (i.e. the increasing oxide layer on the walls) as the FA content increases. The absence of excess O^{-2} at a constant FA content, would favor the rate of chemical etching as anodization period increases. Thus, wall thickness would be expected to decrease as well.

ZrO_2 nanotube arrays were also synthesized using different applied anodization voltages (10-50V) while keeping all other anodization parameters intact. Fig. S4 shows the grown nanotubes at 10 and 30V. While no nanotube structures were observed at 10V, increasing the voltage resulted in the formation of nanotube arrays with larger tube diameters of 25 and 82 ± 1 nm for 30 and 50V, respectively. The nanotubes synthesized at 30 and 50V had a nearly-identical wall thickness of 10.5 ± 1 nm. The tube length, however, showed an increase until an applied potential of 30V reaching a length of 40 ± 0.2 μm, in agreement with Wang and Luo.[27] This increase in length was followed by a shallow decrease to 24 ± 0.2 μm as the applied voltage increased to 50V.

3.2 Proposed Anodization Model

Herein, we present a model for the synthesis of ZrO_2 nanotubes via anodic oxidation that fits the obtained results in this and other studies. According to the second and third generations of the Point Defect Model (PDM II-III),[30,32,33] high oxidation state metals, such as Zr, form a bi-layer passive film composed of a barrier layer, and an outer layer where film/electrolyte interactions occur. The growth of both layers depends on the constant generation and annihilation of cation interstitials and anion vacancies. Macdonald *et al.*[34] studied the impedance characteristics of Zr metal immersed in aqueous de-aerated solutions, and concluded the formation of an oxide outer layer, on top of a defective oxide barrier layer. In a later study, Macdonald and Engelhardt[33] studied the bi-layer passive film forming on Zr in hydride-rich solutions, and concluded the formation of a hydride instead of an oxide barrier layer, owing to the faster diffusion kinetics of hydrogen as compared to oxygen. In this sense, F^- ions are almost twice as fast as O^{2-} ions.[35] Therefore, it is reasonable to assume the formation of a fluoride barrier layer when Zr metal is immersed in fluoride-rich electrolytes.

As immersing the Zr foil into the electrolyte, a defective fluoride layer starts to build up into the metal surface as a result of the constant generation of fluoride vacancies at the foil/electrolyte interface, i.e.,

$$Zr \rightarrow Zr_{Zr} + 2V_F^{\cdot} + 2e^- \quad (2)$$

$$V_F^{\cdot} + NH_4F \rightarrow F_F + NH_4^+(aq) \quad (3)$$

On the other hand, field-assisted dissolution of the barrier layer occurs causing the decrease in the barrier layer thickness (i.e. de-passivation),[27,30] i.e.,

$$ZrF_2 + 4F^- + 2H^+ \rightarrow H_2ZrF_6 \quad (4)$$

In reaction 4, the formation of fluorozirconic acid (H_2ZrF_6) is the most probable route for Zr metal in fluoride-containing aqueous solutions.[36,37] The net thickness of the steady state fluoride barrier layer depends on the fluoride concentration, voltage, pH, and the standard rate constants of the passivation/de-passivation reactions.[32] Indeed, the formation of a fluoride-rich layer at the oxide/metal interface has been reported for Zr,[38] as well as Tantalum.[39,40] Meanwhile, cation interstitials, ejected from the foil's surface, diffuse through the barrier layer towards the barrier layer/electrolyte interface. They then get hydrated/oxidized *via* the anions in the electrolyte, forming oxides (outer layer),[30] i.e.,

$$Zr \rightarrow Zr_i^{''''} + 4e^- \quad (5)$$

$$Zr_i^{''''} + H_2O \rightarrow 2H^+ + ZrO^{2+} \quad (6)$$

$$ZrO^{2+} + H_2O \rightarrow 2H^+ + ZrO_2 \quad (7)$$

In addition, field-assisted dissolution (reaction 8) and chemical etching (reaction 9) create pits on top of the metastable outer layer, i.e.,

$$ZrO_2 + 2H^+ \rightarrow ZrO^{2+} + H_2O \quad (8)$$

$$ZrO_2 + 6F^- + 4H^+ \rightarrow [ZrF_6]^{2-} + 2H_2O \quad (9)$$

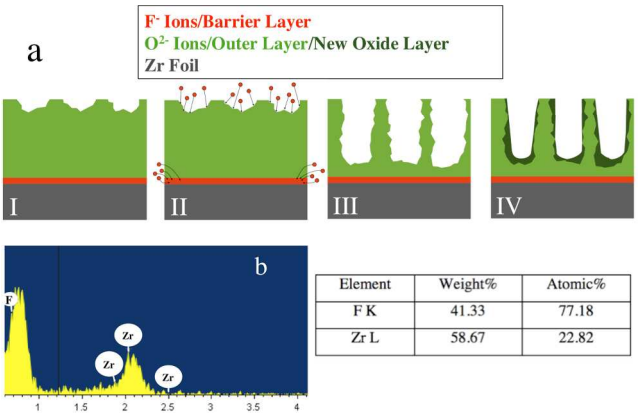

Element	Weight%	Atomic%
F K	41.33	77.18
Zr L	58.67	22.82

Fig. 2 (a) A schematic illustrating the anodization of Zr foils in fluoride-rich electrolytes. (b) EDX spectra of the bottoms of detached nanotubes showing a F^- ion at% almost double that of Zr.

Fig. 2(a) schematically depicts our proposed model. The thickness of the outer layer can surpass that of the barrier layer by 4 orders of magnitude, which is typical for anodization of valve metals.[30] Field-assisted dissolution of the outer layer results in surface irregularities, where fluoride ions then locally decrease the thickness of the layer through pitting action on the rough surface[21] causing an increase in the electric current across it. This triggers more oxide precipitation at the areas where outer layer thickness is decreased.[20] The latter also occurs on the inner walls of the pores,[41] resulting in the formation of well-defined nanotube structures.

Thus, the abundance of F^- and O^{2-} ions is crucial for the formation of ZrO_2 nanotubes with high structural integrity. When 0.5wt% NH_4F was used in the anodization electrolyte, F^- ion content was too low to form well-defined nanotubes, especially at low water contents, and a poorly-structured layer of amorphous debris covered the nanotube arrays (Fig. S1). On the other hand, when the F^- ion content was too high, increased F^- ion diffusion towards the metal/barrier layer interface leads to the detachment of the outer nanotubular layer, as previously observed with Tantalum,[35,40] leading to a decreased nanotube length as mentioned above. Indeed, EDX analysis of the bottoms of the detached nanotube arrays (Fig. 2(b)) showed a non-stoichiometric layer of ZrF_2. Increasing FA content caused the acceleration of both F^- and O^{2-} ions, thus shifting the reactions equilibria forward, and increasing the rate of nanotube formation.

With respect to increasing the voltage, PDM-II[32] predicts the dependence of the steady state barrier layer thickness (L_{SS}) on the applied voltage, i.e.,

$$L_{SS} \propto \frac{1}{\varepsilon}\left[1 - \alpha - \frac{\alpha\alpha_d}{\alpha_p}\right]V \quad (10)$$

such that ε is the electric field strength, α is the polarizability of the barrier layer/outer layer interface, α_p and α_d are the transfer coefficients of the passivation and de-passivation reactions. Eq. 10 entails the increase in the fluoride barrier layer thickness as the applied voltage increases. As a result, at high enough voltages (above 30V), the impedance of the barrier layer becomes no longer negligible with respect to that of the outer layer. This may hinder the diffusion of cation interstitials throughout the barrier layer, thus decreasing the kinetics of nanotube formation into the

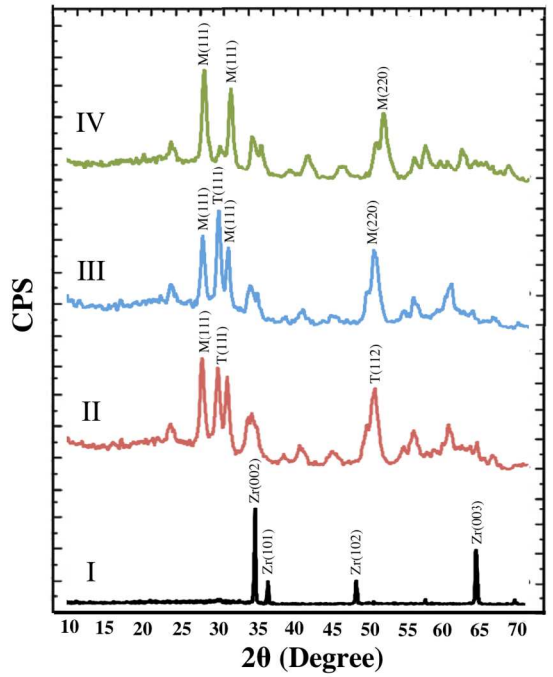

Fig. 3 XRD spectra of (I) as-anodized nanotube arrays, and (II-IV) as-annealed nanotube arrays (500^0C – 4 h) synthesized in glycerol electrolytes containing 0%, 20%, and 40% FA, respectively. M=Monoclinic Phase; T=Tetragonal Phase.

outer layer, and resulting in shorter nanotubes for higher applied potentials.

3.3 Crystallization of the Nanotubes

The nanotube arrays synthesized in electrolytes containing different FA contents were annealed at 500°C in air. X-ray diffraction patterns of as-anodized and annealed nanotube arrays are shown in Fig. 3. The as-anodized nanotubes are amorphous, with some peaks appearing at 35°, 37°, 48°, and 64° characteristic of the (002), (101), (102), and (003) facets of hexagonal Zr metal.[22] These peaks possibly originated form the substrate. In addition, a trace broad peak lies in the region between 28° and 32°. After annealing, this broad peak is de-convoluted showing three distinct peaks at 28°, 30°, and 31°, which correspond to the (111) facet in the monoclinic oxide phase (28° and 31°) and the (111) facet in the tetragonal oxide phase (30°) (27,28). Smaller peaks appear near 50°, which correspond to the (220) and (022) facets in the monoclinic oxide phase,[22] as well as the (112) facet in the tetragonal oxide phase.[27] Note the absence of the characteristic tetragonal phase at 30° in the annealed samples originally grown in electrolytes containing 40% FA. Thus, XRD patterns confirm the formation of ZrO_2 nanotubes with dominating monoclinic phase.

3.4 Energy Considerations

To formulate a market-reliable synthesis protocol for ZrO_2 nanotubes, the total energy used for their synthesis should be calculated. Herein, we calculated the energy required for the individual processes occurring inside the electrolyte during the synthesis process. To this end, the anodization process can be divided into two major processes: (1) the chemical synthesis and dissolution of the oxide layer, and (2) the physical diffusion of ions near the electrolyte/anode interface. The chemical process represented by the formation of the bi-layer passive film at the anode, as well as the evolution of H_2 at the cathode can be combined in an overall reaction as follows:

$$2Zr(s) + 2H_2O(l) + 2NH_4F(aq) \Rightarrow ZrF_2(s) + ZrO_2(s) + 2H_2(g) + 2NH_4^+(aq) \quad (11)$$

Following Li's model,[42] the minimum work (W) associated with the chemical synthesis can be described as:

$$W = (H_R - TS_R) - (H_P - TS_P) \quad (12)$$

which gives roughly 498.533 kJ/mol[43] for anodization of Zr foils. This represents the amount of energy needed for the overall reaction to occur when reversible reactions are ignored. On the other hand, the dissolution of the barrier and outer layers is described by reactions 3 and 8, respectively. Considering the two reactions as different routes for the formation of the $[ZrF_6]^{2-}$ complex, the total energy of formation for both reactions is 395.616 kJ/mol.[43,44]

The electrical energy required for the physical diffusion of ions near the electrolyte/anode interface under applied potential V for time t can be given by:[42]

$$E = V \times A \times I \times t \quad (13)$$

$$I = \frac{nPFDC_0}{L + Px_0} \quad (14)$$

where A is the electrode surface area, P is the porosity of the nanotube array, F is Faraday's constant, D is the diffusion coefficient of ions inside the electrolyte, and C_0 is the concentration of F^- ions inside the bulk electrolyte away from the diffusion layer. L and x_0 are the array thickness and diffusion layer thickness, respectively. Finally, n is the number of exchanged electrons in the overall process. The porosity of the nanotube samples was calculated for nanotubes with circular cross section (Fig. 1(c)) to be 44.9%. Following Li's approach,[42] the diffusion coefficient for F^- ions inside the electrolyte was taken to be 10^{-5} cm^2/sec, and x_0 was to set to be 10.5 µm. With the nanotube length of 24 µm, and C_0 of 3.4×10^{-4} mol/cm^3, the energy required for the physical diffusion of F^- ions near the anode surface is about 110,799.436 kJ/mol.

Thus, the total energy required for the synthesis of ZrO_2 nanotubes via anodization of Zr foils is estimated as 111,693.6 kJ/mol, with the physical diffusion of ions inside the electrolyte being the most energy-consuming step in the anodization process.

3.5 Optical Properties

To investigate the optical characteristics of anodized ZrO_2 nanotubes, Finite Difference Time Domain (FDTD) calculations were performed, along with experimental characterization for transmittance and absorption of the nanotubes. FDTD is a well-known computational technique that allows the investigation of the optical properties of the nanotubes through observing the propagation of electromagnetic waves throughout the lattice. Along the simulation process, the values for the fields throughout each computational grid are updated, rendering FDTD a very useful tool for the optimization of material optical properties.

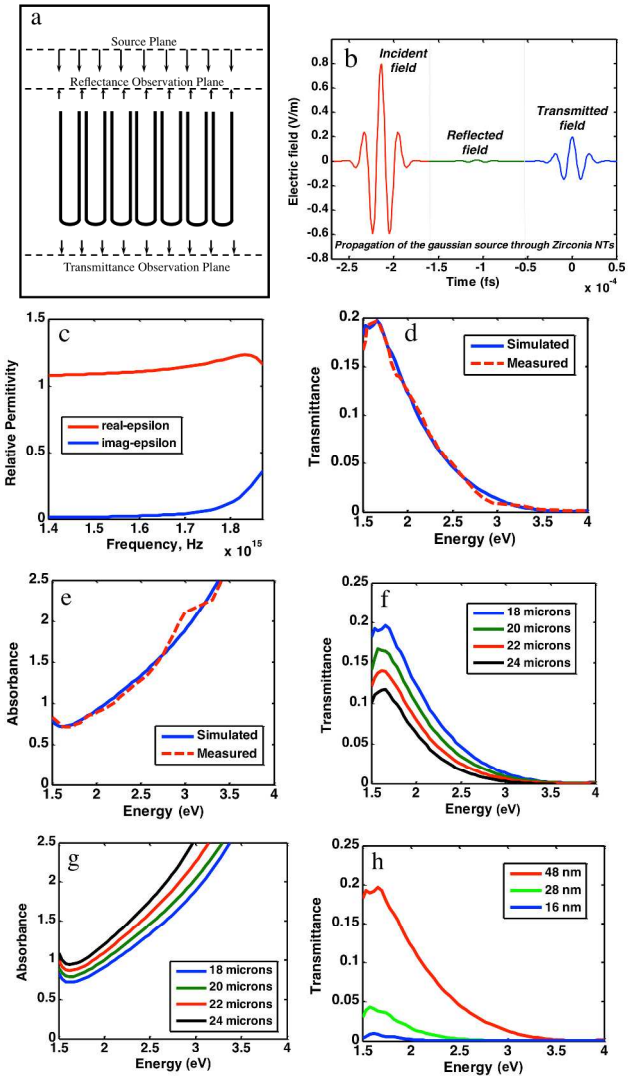

Fig. 4 (a) A schematic showing the model built for the FDTD calculations, (b) A plot showing the incident, reflected, and transmitted electromagnetic fields in the time domain. (c) Dependence of the relative permittivity of ZrO_2 on the frequency of the incident field. (d,e) A comparison between the measured and simulated transmittance and absorption, respectively, for ZrO_2 nanotubes having a length of 18μm, a diameter of 64nm, and a wall thickness of 12nm. (f,g) Simulated data for transmittance and absorption of nanotubes having different lengths. (h) Simulated data for transmittance of nanotubes having different wall thicknesses.

Fig. 4(a,b) illustrates the model used in the FDTD analysis. Following the work of Ong *et al.*,[45] normal incidence of the electromagnetic waves in the negative Z direction was assumed. The model was built for highly-oriented ZrO_2 nanotubes having circular cross-section with an average length of 18μm, an outer diameter of 64nm, and a wall thickness of 12nm. The cell used was surrounded by a matching layer to absorb any reflected electromagnetic waves outside the tubes at all frequencies and angles of incidence.

ZrO_2, being a dispersive material, necessities the accurate calculation of the material's permittivity in order to be able to investigate the optical properties of the nanotubes. For this purpose, density functional theory (DFT) calculations were first performed, using the exchange-correlation functional of Perdew-Burke-Ernzerhof (PBE), to obtain the dielectric function for pure zirconia. Fig. 4(c) shows the real (ε') and imaginary (ε'') parts of the dielectric function together with the operating frequency i.e.

$$\varepsilon' = n^2 - k^2 \quad (15)$$

$$\varepsilon' = 2nk \quad (16)$$

Fig. 4 panels (d,e) show the strong agreement of the measured transmittance and absorbance with the simulated results. Note that the absorbance (A) was measured according to the following relation:

$$A = \left|\log\left(\frac{p_t}{p_i}\right)\right| \quad (17)$$

such that p_t and p_i are the transmitted and incident fields, respectively. Due to the small reflection from the nanotube tops in comparison with the transmitted field, this reflection can be neglected.[45] Fig. 4(f) shows a decrease in the transmittance of the incident field for longer nanotubes, in agreement with other reports in literature.[46,47] This is attributed to the increase of the absorption on the incident field with increasing nanotube length, Fig. 4(g). In addition, Fig. 4(g) shows that the incident field with energy larger than 3.5 eV is totally absorbed by the nanotubes; such observation can be used to get a rough estimate of the ZrO_2 nanotube band gap.

Because the wall thickness of the nanotubes is very crucial when designing photoactive systems, the effect of increasing wall thickness on the optical properties of the ZrO_2 nanotubes was studied using the proposed FDTD model. Fig. 4(h) shows the change in transmittance of the nanotubes as the wall thickness of the nanotubes get thicker, while keeping the outer diameter and the tube length fixed. As shown, the transmittance decreases with increasing the wall thickness of the nanotubes, due to the decrease in the volume of the air column inside the nanotubes, thus increasing the effective index of refraction.[45]

4 Conclusion

In this article, a roadmap for the effect of synthesis parameters on the morphology and optical properties of ZrO_2 nanotubes was presented. Increasing formamide and water contents in the electrolyte, as well as anodization time and voltage till 30V resulted in an increase in the nanotube lengths and diameters, which was attributed to the increased reaction kinetics. Although increasing F^- ion concentration led to increased nanotube diameters, it resulted in a decrease in the length. Similar results were obtained with increasing the anodization potential above 30V. Nanotubes synthesized in O^{-2}-rich electrolytes exhibited thicker tube walls as compared to those synthesized in electrolytes with lower formamide concentrations. The optimum process conditions were defined as follows: for highly-ordered ZrO_2 nanotubes with circular morphology, Zr foils were anodized for 3hrs at 50V in a glycerol-based electrolyte containing 20% FA, 1wt% NH_4F, and 4wt% H_2O. To obtain nanotubes with hexagonal morphology, etchant and water contents were 2wt%. A model for the anodization of Zr foils was proposed based on the Point Defect Model such that a fluoride barrier layer grows into the metal, on top of which an oxide outer layer precipitates. The effect of nanotube dimensions on their optical properties was

studied using FDTD. A good agreement between theoretical and the experimental results allowed for the accurate prediction of the optical properties. Unlike absorption, transmittance of the nanotubes was shown to decrease with nanotube length and wall thickness. The results presented herein provide the general framework for the synthesis of optically-active ZrO_2 nanotubes.

Acknowledgement

This work was made possible by NPRP Grant No. NPRP 6-569-1-112 from the Qatar National Research Fund (a member of Qatar Foundation).

Notes and references

[a]*Energy Materials Laboratory (EML), Physics Department, School of Sciences and Engineering, The American University in Cairo, New Cairo 11835, Egypt; E-mail: nageh.allam@aucegypt.edu*

[b]*Department of Chemistry and Earth Sciences, Qatar University, P. O. Box 110003, Doha, Qatar.*

† Electronic Supplementary Information (ESI) available: the full sets of FESEM images due to the variation in electrolyte composition, applied voltage and anodization time, as well as two tables showing the variation in nanotube dimensions are included. See DOI: 10.1039/b000000x/

1 H. K. Kammler, L. Mädler and S. E. Pratsinis, *Chem. Eng. Technol.*, 2001, **24**, 583-596.
2 C. Suryanarayana, *Mater. Today*, 2005, **8**, 62-62.
3 N. K. Hassan, M. R. Hashim, M. A. Mahdi and N. K. Allam, *ECS J. Solid State Sci. Technol.*, 2012, **1**, P86-P89.
4 V. Lefevre, *Nanowires: properties, synthesis and applications*, Nova Science Publishers, New York, 2012.
5 H. Dai, *Chem. Res.*, 2002, **35**, 1035-1044.
6 S. Hou, C. C. Harrell, L. Trofin, P. Kohli and C. R. Martin, *J. Am. Chem. Soc.*, 2004, **126**, 5674-5675.
7 N. K. Allam, N. M. Diab and N. A. Ghany, *Phys. Chem. Chem. Phys.*, 2013, **15**, 12274-12282.
8 N. K. Allam and C. A. Grimes, *Mater. Lett.*, 2011, **65**, 1949-1955.
9 N. K. Hassan, M. R. Hashim and N. K. Allam, *Physica E*, 2012, **44**, 1853-1856.
10 N. K. Hassan, M. R. Hashim and N. K. Allam, *Chem. Phys. Lett.*, 2012, **549**, 62.
11 A. Fujishima and K. Honda, *Nature*, 1972, **238**, 37-38.
12 K. Shankar, J. I. Basham, N. K. Allam, O. K. Varghese, G. K. Mor, X. Feng, M. Paulose, J. A. Seabold, K. Choi and C. A. Grimes, *J. Phys. Chem. C*, 2009, **113**, 6327–6359.
13 M. Walter, E. Warren, J. McKone, S. Boettcher, Q. Mi, E. Santori and N. S. Lewis, *Chem. Rev.*, 2010, **110**, 6446-6473.
14 M. Das, C. Dhand, G. Sumana, A. K. Srivastava, N. Vijayan, R. Nagarajan, B. D. Malhotra, *Appl. Phys. Lett.*, 2011, **99**, 143702-143703.
15 C. J. Frandsen, K. S. Brammer, K. Noh, L. S. Connelly, S. Oh, L. Chen and S. Jin, *Mater. Sci. & Eng. C* 2011, **31**, 1716-1722.
16 L. Wang and J. Luo, *Mater. Sci. & Eng. C*, 2011, **31**, 748-754.
17 R. Liang, M. Deng, S. Cui, H. Chen and J. Qiu, *Mater. Res. Bull.*, 2010, **45**, 1855-1860.
18 D. Fang, Z. Luo, S. Liu, T. Zeng, L. Liu, J. Xu, Z. Bai and W. Xu, *Opt. Mater.*, 2013, **35**, 1461-1466.
19 X. Wang, J. Zhao, X. Hou, Q. He and C. Tang, C., *J. Nanomater.*, 2012, **2012**, 1-5.
20 S. Ismail, Z. A. Ahmad, A. Berenov and Z. Lockman, *Corros. Sci.*, 2011, **53**, 1156-1164.
21 W. Lee and W. Smyrl, *Curr. Appl. Phys.*, 2008, **8**, 818-821.
22 W. Lee and S. Park, *Chem. Rev.*, 2014, **DOI:** 10.1021/cr500002z.
23 X. H. Huang, G. H. Li, X. C. Dou, and L. Li, *J. Appl. Phys.* 2009, **105**, 084306.
24 F. Muratore, A. Baron-Wiechec, T. Hashimoto, P. Skeldon and G. E. Thompson, *Electrochem. Commun.*, 2010, **12**, 1727-1730.
25 H. Tsuchiya, J. M. Macak, L. Taveira and P. Schmuki, *Chem. Phys. Lett.*, 2005, **410**, 188-191.
26 J. Zhao, R. Xu, X. Wang and Y. Li, *Corros. Sci.*, 2008, **50**, 1593-1597.
27 X. Ying, L. Xuan-Yong and D. Chuan-Xian, *J. Inorg. Mater.*, 2012, **27**, 107-112.
28 L. Wang and J. Luo, *J. Phys. D: Appl. Phys.*, 2011, **44**, *075301*
29 J. Zhao, X. Wang, R. Xu, F. Meng, L. Guo and Y. Li, *Mater. Lett.*, 2008, **62**, 4428-4430.
30 D. D. Macdonald, *Electrochim. Acta*, 2011, **56**, 1761-1772.
31 H. Habazaki, K. Fushimi, K. Shimizu, P. Skeldon and G. E. Thompson, *Electrochem. Commun.*, 2007, **9**, 1222-1227.
32 D. D. Macdonald, *Appl. Chem.*, 1999, **71**, 951-978.
33 D. D. Macdonald and G. R. Engelhardt, *ECS Trans.*, 2010, **28**, 123-144.
34 J. Ai, Y. Chen, M. Urquidi-Macdonald and D. D. Macdonald, *J. Nucl. Mater.*, 2008, **379**, 162-168.
35 N. K. Allam, X. J. Feng and C. A. Grimes, *Chem. Mater.*, 2008, **20**, 6477-6481.
36 M. E. Straumanis and J. I. Ballass, *Z. anorg. allgem. Chem.*, 1955, **278**, 33-41.
37 W. B. Blumenthal, *The Chemical Behavior of Zirconium*, D. Van Nostrand Company, Inc., New Jersey, 1958, p 136.
38 D. Fang, J. Yu, Z. Luo, S. Liu, K. Huang and W. Xu, *J. Solid State Electrochem.*, 2012, **16**, 1219-1228.
39 R. E. Pawel, J. P. Pemsler and C. A. Evans, Jr., *J. Electrochem. Soc.*, 1972, **119**, 24-29.
40 K. Shimizu, K. Kobayashi, G. E. Thompson, P. Skeldon and G. C. Wood, *J. Electrochem. Soc.*, 1997, **144**, 418-423.
41 D. Regonini, C. R. Bowen, A. Jaroenworaluc and R. Stevens, *Mater. Sci. Eng. Rep.*, 2013, **74**, 377-406.
42 B. Li, X. Gao, H. Zhang and C. Yuan, *ACS Sustainable Chem. Eng.*, 2014, **2**, 404-410.
43 M. W. Chase, Jr., *J. Phys. & Chem. Ref. Data*, 1986, **14**, 1-1856.
44 E. I. Voit, A. V. Voit and V. I. Sergienko, *Glass Phys. & Chem.*, 2001, **27**, 195-203.
45 K. G. Ong, O. K. Varghese, G. K. Mor and C. A. Grimes, *J. Nanosci. & Nanotechnol.*, 2005, **5**, 1801-1808.
46 N. Nigishi, K. Takeuchi and T. Ibusuki, *J. Mater. Sci.*, 1998, **33**, 5789-5794.
47 F. M. Amanullah, M. S. Al-Mobarak, A. M. Al-Dhafiri and K. M. Al-Shibani, *Mater. Chem. Phys.*, 1999, **59**, 247-253.